Anisotropy-driven magnetic structures in manganese ferrite nanoparticle assemblies

Y. Ijiri,[1,*] J. A. Borchers,[2] K. L. Krycka,[2] A. Khelil,[1] T. Coulson,[1]
S. Siegel,[1] N. Vanderloo,[1] S. A. Sabol-Pulling,[1] N. J. Talmor,[1]
H. Chen,[3] J. J. Rhyne,[2] V. K. Lazarov,[4] and S. A. Majetich[3]

[1] *Oberlin College, Department of Physics and Astronomy, Oberlin, OH 44074*
[2] *National Institute of Standards and Technology,*
NIST Center for Neutron Research, Gaithersburg, MD 20899
[3] *Carnegie Mellon University, Department of Physics, Pittsburgh, PA 15213*
[4] *University of York, School of Physics,*
Engineering and Technology, Heslington, York, YO10 5DD, UK

(Dated: August 26, 2026)

Abstract

Polarization-analyzed small-angle neutron scattering (PASANS) methods are used to determine the spin arrangements and experimental length scales of magnetic correlations in ordered three-dimensional assemblies of ~ 7.6 nm diameter chemically homogeneous manganese ferrite nanoparticles. While the perpendicular magnetic scattering at remanence mostly follows single particle behavior at high temperature, the scattering deviates upon cooling the particles, growing maximally at intermediate temperatures ($\approx$ 50-100 K) with intermediate field values also displaying canted magnetic structures. The data are fit with a sphere-based mass fractal model and are interpreted further via a micromagnetic simulation approach. The unusual temperature and field dependencies are explained in terms of a delicate balance between magnetic anisotropy and demagnetization. These results highlight the ability of PASANS to extract key features in nanoscale systems and the importance of correlating micromagnetic simulations.

I. INTRODUCTION

Magnetic nanoparticles continue to be of great interest [1, 2] due to their long-recognized importance in applications ranging from data storage to biomedical diagnostics and therapy to environmental remediation [3–6]. Recent experiments have highlighted the tunability of magnetic behavior in ordered dense assemblies of magnetite (Fe_3O_4) nanoparticles, either with controlled spacing variation [7] or under pressure [8]. On the theoretical side, research continues to bridge the gap from local spin models and assumed interparticle interactions to observed macroscopic behavior [9, 10]. To advance this research, a key need is to characterize the complex spin structures involved and pinpoint the underlying controlling mechanisms.

Neutron scattering techniques have been demonstrated to be very effective magnetic ordering probes for powdered oxide nanoparticle collections [11–24]. In particular, full polarization-analyzed small-angle neutron scattering (PASANS) techniques [25–27] allow for explicit separation of 3D structural versus magnetic features over a wide range of temperature and field conditions.

In previous PASANS work, we have shown that dense collections of ordered ferrite nanoparticles can exhibit a range of behavior, depending on the balance of relevant en-

* yumi.ijiri@oberlin.edu

ergy terms [15, 18, 19, 21, 23]. In $CoFe_2O_4$ assemblies, the very high magnetocrystalline anisotropy along with Zeeman energy in a field led to mostly single particle alignment with a canting of spins that is incoherent from nanoparticle to nanoparticle [18]. In the case of Fe_3O_4, exchange and Zeeman energies were the most important, driving the formation of a magnetic core and shell that changed with field and temperature, despite a uniform nanoparticle structure [15, 19]. Chemically distinct core-shell $Fe_3O_4/Mn_xFe_{3-x}O_4$ nanoparticles with lower anisotropy [21, 23] were shown to have appreciable spin canting within each nanoparticle and with the canting even coherent from nanoparticle to nanoparticle over significant length scales. In that case, the unusual intraparticle order was attributed in part to the Dzyaloshinskii-Moriya interaction with structural stacking faults and interparticle dipolar coupling leading to the longer range order. However, the complex core-shell morphology of these nanoparticles impeded further, more quantitative analysis of the underlying mechanisms.

Here, we focus on a simpler version of ordered assemblies of manganese ferrite nanoparticles in which special care has been taken to ensure phase homogeneity. This system is of particular interest as a result of the biocompatibility of manganese and tunability of the material with respect to changes in the average particle size, surface ligand, or possible core-shell morphology [28–31]. Manganese ferrite itself is well-known to have a significant sensitivity to Mn-Fe stoichiometry, resulting in substantial, non-monotonically varying changes to its soft magnetic anisotropy as a function of temperature [32–34], with values in the bulk ranging from $\approx$ 1-20 kJ/m^3 in the temperature range of interest.

We find that although the magnetic scattering is generally much more straightforward than for other ferrite nanoparticle systems, there is an unusual deviation from single particle behavior which maximizes at intermediate temperatures. The perpendicular magnetic scattering mimics a fractal system with a length scale corresponding to correlations of several nanoparticles and fractal dimension values varying from one to two upon cooling. In addition, intermediate field conditions are observed to promote a canted, multi-particle magnetic structure. The results are interpreted in terms of a series of micromagnetic simulations which highlight the key role of magnetic anisotropy in dictating the relevant dipolar-stabilized structures.

II. METHODS

The manganese ferrite nanoparticles for this investigation were prepared by high temperature non-aqueous solution chemistry methods mostly as previously described, with oleic acid as the surfactant to prevent particle agglomeration [35]. In order to compensate for the large difference in the decomposition temperatures of the iron and manganese precursors, both materials were pre-heated and injected hot into the reaction vessel to promote chemical uniformity throughout the nanoparticles. Nanoparticle size and chemical homogeneity were probed via transmission electron microscopy (TEM) and high-angle annular dark field (HAADF) scanning transmission electron microscopy (STEM) coupled with electron energy loss spectroscopy (EELS). Atomic absorption spectroscopy was used to quantify the Mn to Fe ratio.

Standard magnetic susceptibility versus temperature and magnetization versus applied field measurements were taken using a vibrating sample magnetometer at temperatures ranging from 10 K to 300 K and fields from 0 to 3 T to confirm the overall magnetic behavior and to guide neutron scattering measurements.

Through a combination of alcohols with different solubilities for the particles [36, 37], the nanoparticles were self-assembled into dense arrays, coming out of solution over the course of weeks. While the explicit form of close-packing was not measured for this sample, previous small-angle x-ray scattering work on related particles showed face-centered cubic (FCC) stacking instead of hexagonal close-packed (HCP) stacking when slow precipitation methods were used [37–39]. No applied magnetic field was used in the crystal formation process. After crystallization, the resulting powder of dense arrays of nanoparticles was sealed in aluminum cells for neutron scattering measurements.

PASANS experiments were performed at the NIST Center for Neutron Research on the vSANS instrument which allows for simultaneous collection of data from several sets of detector banks. As depicted in Figure 1, the vSANS instrument includes an in-beam FeSi supermirror polarizer cavity to polarize the incident neutrons, a radio frequency spin flipper to switch the polarization of the incident neutrons, and a polarized ^{3}He cell in transmission geometry as a spin analyzer equipped with an in-situ NMR flipper for the scattered neutrons as described in earlier work [40, 41].

The sample temperature was adjusted in a closed-cycle He refrigerator from 5-415 K, and

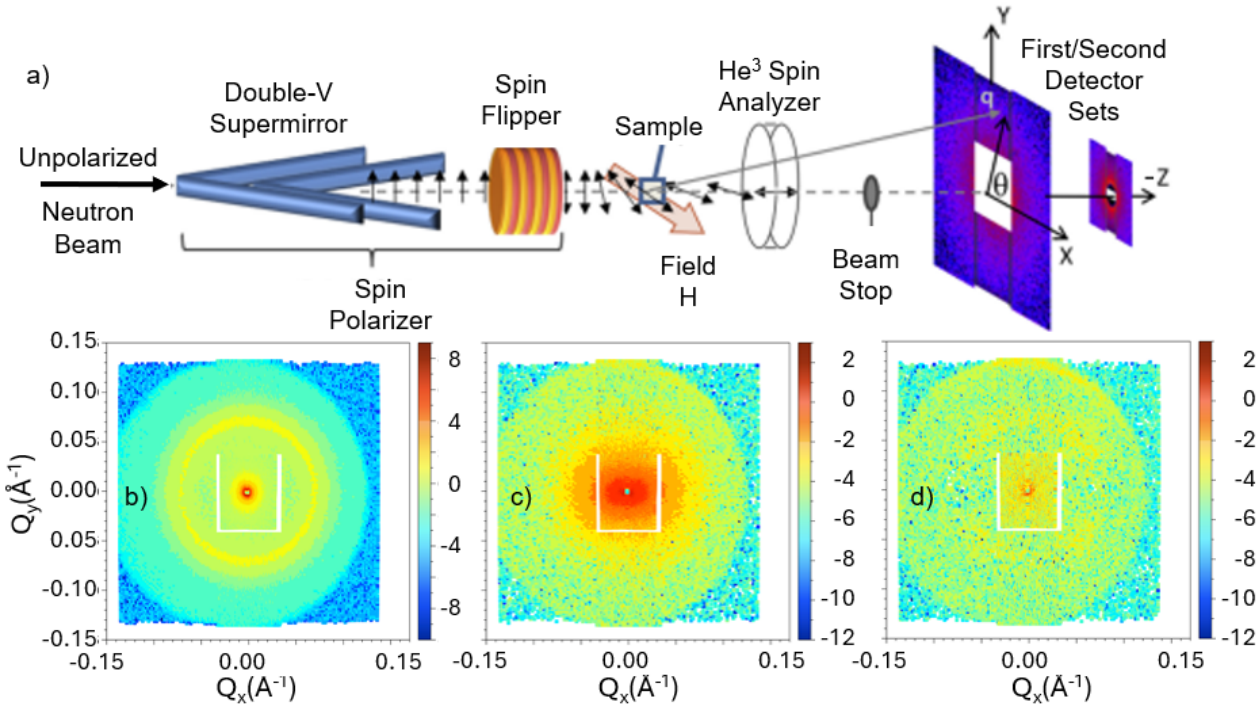


FIG. 1. a) vSANS experimental setup depicting key neutron spin components. Illustrative two-dimensional data at 5 K for b) a non-spin flip cross-section in remanence c) a spin flip cross-section in remanence and d) a spin flip cross-section in 1.4 T. White lines indicate masking at detector overlap regions. The intensity data have been scaled against an empty beam.

an electromagnet was used to apply magnetic fields ($\mu_o H$) up to 1.4 T, which for these dense arrays of nanoparticles yield magnetization values that are very close to fully saturated based on magnetometry data. Data were collected simultaneously in transmission with the front and middle detector banks to span the scattering vector $\vec{Q}$ range from ≈ 0.005 Å^{-1} to 0.125 Å^{-1}, probing structures on the order of 5-150 nm. Figure 1 also indicates the orientation with the neutron beam along Z, the applied field along X, the detector in the $X-Y$ plane, and the angle θ between $\vec{Q}$ and X. Note that the magnitude of $|\vec{Q}|= 4\pi \sin(\phi)/\lambda$, with 2ϕ, the scattering angle between source and detector and λ, the neutron wavelength.

Corrections for the time-dependent decay of the ^{3}He polarization, inefficiencies in the supermirror and flippers, and detector inhomogeneities were made, and the data were reduced following procedures outlined previously [26, 42]. With the direction of the neutron spin relative to the polarization axis denoted as + or -, applying these corrections then yielded the intensity measurements of all four neutron spin cross-sections (I^{++}, I^{--}, I^{+-}, and I^{-+})

corresponding to either initially + or - spin state neutrons scattering into + or - neutrons. Fig. 1b)-d) show examples of the reduced neutron spin cross-section data taken at 5 K in either a residual remanent field of ~ 0.005 T or in 1.4 T.

The corrected scattering intensities I for the four different polarization conditions are proportional to squared combinations of the nuclear and magnetic structure factors of the sample, taking into consideration the individual scattering strength of the nanoparticles. In addition, the directional dependence of the neutron interaction with magnetic moments is important, as the magnetic scattering is only sensitive to the moment projection perpendicular to the scattering vector Q [25, 26]. Since the sample is isotropic, the nuclear component can be represented by a single isotropic spatial Fourier transform N, while there are three magnetic analogues, M_X, M_Y, and M_Z.

While the expressions to isolate components can be quite complex, they simplify for the geometry depicted in Fig. 1 and certain key angles and assumptions [26]. Again, since the sample consists of crystalline grains of close-packed nanoparticles, but with no distinct orientation from grain to grain, the structural component can be extracted simply from a portion of the non-spin flip (NSF) scattering intensities:

$$N^2 \equiv |N(\vec{Q})|^2 = I^{++}_{\theta=0^\circ}(\vec{Q}) + I^{--}_{\theta=0^\circ}(\vec{Q}), \tag{1}$$

using area-normalized sector slices of $\pm 10^\circ$ taken from $\theta = 0^\circ$, e.g. along the field direction X as indicated in Fig. 1.

In analogy to traditional magnetometry measurements, the NSF scattering data can also be used to probe the net magnetic component parallel to the field direction, $\mathrm{M}^2_{||,net}$ by taking different sector cuts relative to the structural data:

$$M^2_{||,net} \equiv |M_{X,net}(\vec{Q}, 90^\circ)|^2 = \frac{|I^{--}_{\theta=90^\circ}(\vec{Q}) - I^{++}_{\theta=90^\circ}(\vec{Q})|^2}{4N^2}. \tag{2}$$

Note that this simplified expression relies only on the structural uniformity of the sample and no additional assumption on the magnetic ordering [26].

More importantly, the spin flip (SF) scattering data, I^{+-} and I^{-+}, relate *directly* to the other magnetic Fourier transform components, with no structural component whatsoever. Assuming isotropic magnetic scattering perpendicular to the applied field such that $|M_\perp|(\vec{Q})|^2 \equiv |M_Y(\vec{Q})|^2 = |M_Z(\vec{Q})|^2$, we find that

$$
\begin{aligned}
M_{\perp}^{2} \equiv & \frac{I_{\theta=0^{\circ}}^{+-}(\vec{Q}) + I_{\theta=0^{\circ}}^{-+}(\vec{Q}) + I_{\theta=90^{\circ}}^{+-}(\vec{Q}) + I_{\theta=90^{\circ}}^{-+}(\vec{Q})}{3} \\
= & \frac{|M_{Y}(\vec{Q}, 0^{\circ})|^{2} + |M_{Z}(\vec{Q}, 0^{\circ})|^{2} + |M_{Z}(\vec{Q}, 90^{\circ})|^{2}}{3}
\end{aligned}
\tag{3}
$$

thereby providing key $\vec{Q}$-dependent and thus spatially-dependent information on magnetic ordering perpendicular to the field direction [43]. These data are typically not accessible by other measurement approaches which average over the whole sample without sensitivity to differences in magnetic local structure.

To aid in the interpretation of the PASANS results, we performed a series of micromagnetic simulations using the Ubermag [44] (Python-based) utilities for OOMMF (Object-Oriented MicroMagnetic Framework) [45] running on a high-performance computing cluster. A single nanoparticle was emulated by breaking it up into nanometer cell sizes in each dimension (0.83 nm $\times$ 0.83 nm $\times$ 0.83 nm), and the spherical shape then was mimicked by the stacked cubes. Since past work indicated FCC stacking for related nanoparticle assemblies [37–39], the simulated nanoparticles were repeated on an appropriate FCC lattice to approximate the observed structural characteristics with a total of 11 layers and 127 close-packed nanoparticles per layer for a total of nearly 1,400 nanoparticles. The space between nanoparticles, occupied by surfactant molecules, was assumed to have no magnetic character. The simulated structure thus consisted of a single crystal of close-packed nanoparticles with no defects or stacking faults; it was presumed to represent the key features of the experimental sample which had multiple nanocrystals oriented randomly in a powder.

Standard energy minimization routines were employed with explicitly Zeeman, exchange, anisotropy, and demagnetization energies considered. The calculations were performed assuming zero temperature, but with the energy parameters adjusted by their temperature dependence, a factor of considerable importance for the anisotropy term in particular. A saturation magnetization M_S value of 3.57×10^5 A/m was used for the majority of the simulations, given that the bulk Curie temperature for manganese ferrite is 573 K [46], well above the experimental temperatures of interest. The exchange constant A was kept fixed at a literature value of 5×10^{-12} J/m [47]. In contrast, the uniaxial anisotropy constant K values were varied from 1 to 20 kJ/m^3 to match the values observed as a function of temperature in bulk manganese ferrite [32–34]. Magnetic fields ranged from 0.005 T to 1 T and were applied either through the layer stack or in the layer plane.

While the true intrinsic magnetocrystalline anisotropy for a spinel manganese ferrite should be cubic [32–34], the anisotropy energy will also be altered by nanoparticle shape and surface effects and thus is often represented by an effective uniaxial anisotropy [48]. Given this complexity, we chose the simplest representation of anisotropy and randomly assigned a given uniaxial anisotropy direction for each nanoparticle, with all the cells within a nanoparticle having the same anisotropy direction but with the direction varying from nanoparticle to nanoparticle. The magnitude of the anisotropy was kept constant for a given simulation, but was varied from simulation to simulation to span the published range of values for the temperature range in question. In this way, the anisotropy constant served as a proxy for temperature in the simulations, given its much stronger variation with temperature in comparison to other parameters like saturation magnetization.

The energy-minimized output files (.omf) were then used as starting configurations for the generic scattering calculator within SasView [49], a small-angle scattering data fitting and analysis software program. To mimic different sample placements, the OOMMF-simulated nanoparticle assembly was oriented in three different perpendicular directions to compute scattering, with the layer stack assembly direction 1) along the neutron beam axis, 2) along the neutron polarization axis, or 3) perpendicular to both. Spin-flip scattering cross-sections were calculated with the same scattering and polarization geometry as in the experimental data.

III. RESULTS

A. Sample characterization

As shown in Figure 2, microscopy data on isolated particles indicate that the Fe and Mn distributions are fairly uniform for this system in contrast to previous work on core-shell particles [21, 23] showing higher abundance of manganese in the shell [50]. The particles had a mean particle diameter of 7.6 nm $\pm$ 1.4 nm based on conventional TEM images. From atomic absorption spectroscopy, the manganese to iron ratio was estimated at $\approx$ 1:1.6 vs. the 1:2 for a perfect, non-defected spinel-type $MnFe_2O_4$.

Magnetometry data indicate the expected magnetic behavior for manganese ferrite nanoparticles in dilute solution. As shown in Figure 3, the maximum of the zero field-

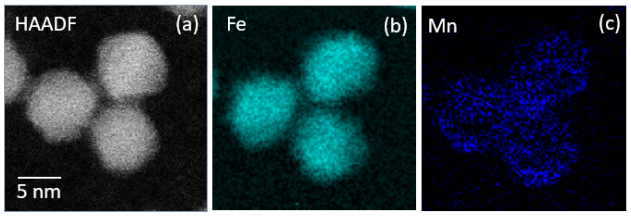


FIG. 2. a) HAADF-STEM images of several isolated nanoparticles along with integrated maps of the b) Fe $L_{2,3}$ EELS signal and c) Mn $L_{2,3}$ EELS signal, showing relatively uniform distributions of Fe and Mn respectively.

cooled susceptibility curve occurs at $\approx$ 35 K, a common indicator of the so-called blocking temperature T_B where the Boltzmann energy ($k_B T_B$) is sufficient to match the anisotropy energy of a particle given by KV where K is the anisotropy constant and V is the volume of the particle. Equating these two energy terms for a T_B of 35 K and considering the particle size distribution determined by TEM, we find that the implied effective anisotropy constant is between $\approx$ 1-4 kJ/m^3, consistent with the larger, temperature-dependent observed range of literature values from $\approx$ 1-20 kJ/m^3 [32–34].

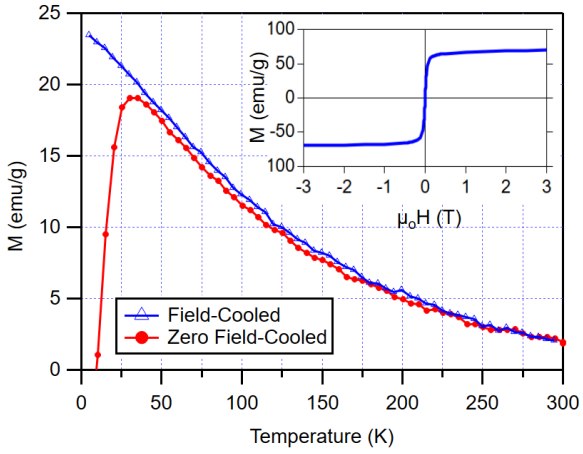


FIG. 3. Comparison of magnetic susceptibility versus temperature for zero field-cooling and for warming after cooling in a 0.01 T field for a dilute solution of the particles. Inset shows the moment behavior of the particles at 10 K as a function of magnetic field.

Based on atomic absorption spectroscopy measurements for the Mn and Fe content and assuming the bulk density for $MnFe_2O_4$, the data in the inset to Fig. 3 indicate a low temperature saturation magnetization of $\approx$ 70 emu/g, roughly 80% of that observed for

bulk single crystal behavior [51]. This reduction is expected to stem from the off-perfect stoichiometry of the nanoparticles.

B. Neutron Scattering

Figure 4 shows the structural scattering extracted using Eq. 1 on the NSF PASANS data illustrated in Fig. 1b). Reflecting the ring of scattering in Fig. 1b), the dominant feature for these nanoparticles is a peak at Q $\approx$ 0.065–0.072 Å^{-1} stemming from structural order that persists over multiple nanoparticles in these dense, self-assembled collections. From 5–200 K, this Bragg peak remains constant with temperature and matches to that expected for an FCC lattice of nanoparticles with lattice parameter of 13.6 ± 0.1 nm and with the peak broadening likely originating from the presence of stacking faults and other defects in the structure. As shown more clearly in the inset, at higher temperatures from 300–415 K, the peak broadens even more and shifts to lower Q, indicating larger, more disordered length scales. This change is consistent with the oleic acid surfactant molecules that surround the nanoparticles becoming floppier and more disentangled, with the lattice parameter thus increasing to 14.2 ± 0.1 nm at the highest temperature. Within measurement uncertainties, no field-dependent changes to the structure are observed. The observed structure matches with that seen in a range of other dense nanoparticle systems consisting of analogous oxides such as $Fe_3O_4/MnFe_2O_4$ [23],$CoFe_2O_4$ [18], Fe_3O_4 [15], or even non-magnetic nanoparticles such as CdSe [36].

While the structural features remain mostly unchanged with only minor modifications above room temperature, the magnetic scattering shows much more variation with field and temperature. In the NSF PASANS data illustrated in Fig. 1b), the magnetic signature $M^2_{||,net}$ extracted from Eq. 2 is evident in the distorted ring shape. The SF PASANS data which are sensitive only to magnetic scattering show clear differences in applied field as depicted in Fig. 1c) and d); these data were used to determine $M^2_{\perp}$ using Eq. 3.

Figure 5 plots the extracted $M^2_{||,net}$ and $M^2_{\perp}$ intensities as a function of Q for several magnetic field values at 200 K, with data at 1.4 T and 5 K for comparison. As shown in Fig. 5a), the net parallel magnetic component mimics the structural ordering peak, indicating that the net magnetization is aligned over many nanoparticles. Fields of 0.1–0.5 T produce very similar scattering curves, with intensity increasing as the field is increased to nearly

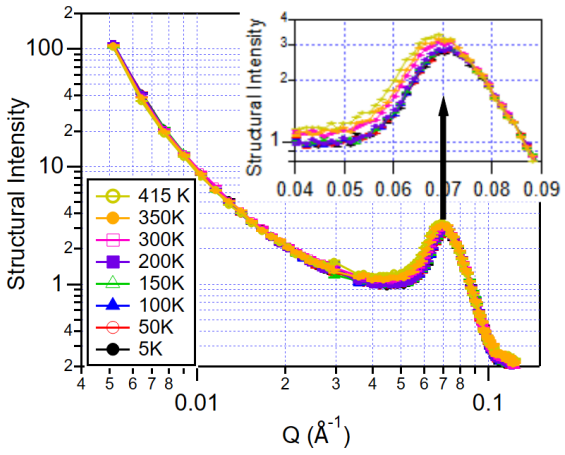


FIG. 4. Data for extracted PASANS N^2 structural intensity using Eqn. 1 vs. scattering vector Q in remanence for temperatures ranging from 5-415 K. Inset illustrates the shift in structural scattering as the surfactant molecules become less rigid from 300 K and above. Error bars in the plot denote standard uncertainties.

match the lowest temperature (5 K), highest field (1.4 T) data. In remanence at 200 K, there is still some net parallel magnetic component that follows the structure, albeit with much lower intensity. These data match to the behavior one would expect for a soft magnetic material as indicated in the inset of Fig. 3.

Note that the $M^2_{||,net}$ signal provides only a partial picture of the true magnetic behavior; as shown in Fig. 5b), $M^2_{\perp}$ has a much richer Q dependence for the same conditions and, in fact, inversely tracks the behavior of the net magnetization parallel to the field. At 5 K and 1.4 T, where the $M^2_{||,net}$ signal is strongest, the $M^2_{\perp}$ scattering is weakest and nearly flat, indicating that nearly all spins are aligned with the field. However, the $M^2_{\perp}$ signal grows with decreasing field but with a more complicated Q dependence that does not simply match that of the close-packed structure of the nanoparticle arrays.

To further characterize the magnetic behavior, in Figure 6 we plot the $M^2_{\perp}$ intensity versus Q for a range of temperatures in a residual remanent magnetic field of ~ 0.005 T. At the highest temperature value of 415 K, the observed scattering signal is mostly described (black dashed line) by a simple model of a non-interacting magnetic sphere with a diameter matching the 7.6 nm result from TEM data [49, 52, 53]. Intuitively, such a model makes sense in that while the particles are in a close-packed assembly, at high temperature and

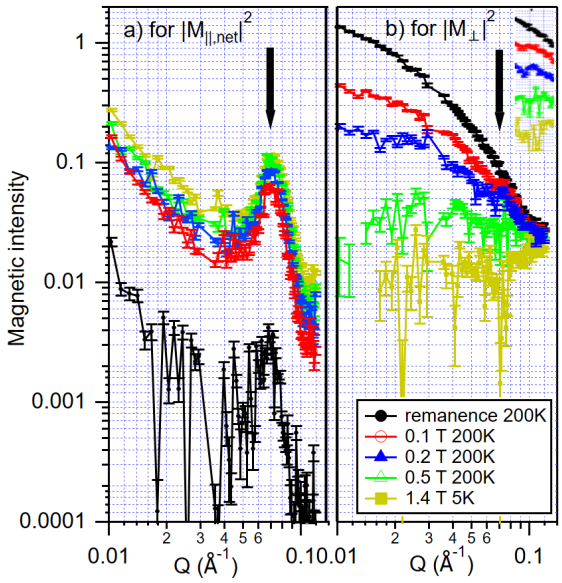


FIG. 5. Data for extracted PASANS intensity a) $M^2_{||,net}$ using Eqn. 2 and b) $M^2_{\perp}$ using Eqn. 3 versus scattering vector Q for 200 K and magnetic fields ranging from remanence to 0.5 T. Data at 1.4 T and 5 K are shown for comparison. Arrows highlight the structural interparticle peak location of 0.07 Å^{-1}. Inset in b) shows $M^2_{\perp}$ data in that region offset for clarity. Error bars in the plot denote standard uncertainties.

minimal field, it is quite plausible that they act independently. Thus, the nanoparticles each have uniform magnetization but with random orientation from nanoparticle to nanoparticle and no interparticle magnetic interactions.

Upon cooling, we would expect to observe additional magnetic scattering intensity as a result of more collective ordering in the perpendicular magnetization, and in general, Fig. 6 shows the anticipated increase with decreasing temperature. However, an anomaly in the temperature dependence is observed as the intermediate temperature conditions ($\approx$ 50-100 K) display the highest intensity with also a pronounced change in the shape of the scattering curve [56].

We note that the observed dependence is reminiscent of the zero field-cooled susceptibility data in Fig. 3 with a blocking temperature of $\approx$ 35 K. However, the time scales for the magnetometry measurements versus the neutron scattering experiments are different. The samples are also not identical: particles in dilute solution vs. polycrystals of dense assemblies. In that regard, more careful consideration is needed to explain the unusual

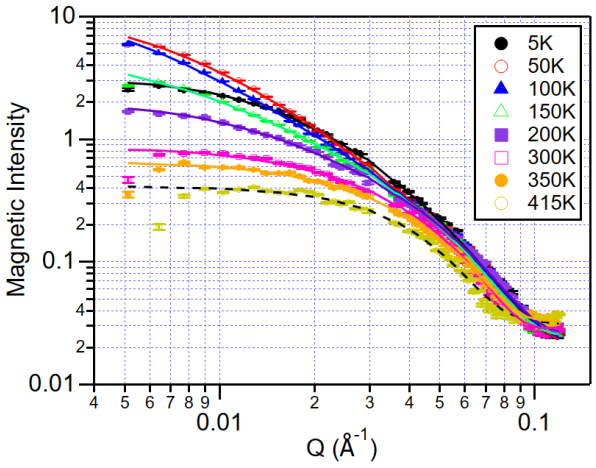


FIG. 6. Data for extracted PASANS intensity $M_{\perp}^2$ using Eqn. 3 versus scattering vector Q for temperatures from 5-415 K in remanent magnetic field. Dashed line for 415 K represents the expected scattering form factor for 7.6 nm diameter non-interacting spheres. Solid lines represent fit with mass fractal model described in [49, 54, 55] applied. Error bars in the plot denote standard uncertainties.

temperature dependence.

To further interpret the temperature-dependent magnetic scattering data, we have applied a mass fractal model that is often used to describe particulate systems that show fractal behavior with a characteristic dimension over a certain maximum correlation length [49, 54, 55, 57]. Originally used to understand the structural properties of silica particles and other aggregates, the model has also been applied to characterize the structural clustering of magnetic nanoparticles and ferrofluids [58, 59] and more recently for magnetic skyrmions in Fe/Gd multilayers [60].

Here, we fit the perpendicular magnetic scattering to the mass fractal model as shown in the solid lines in Fig. 6. In Figure 7, we plot for the data at different temperatures, the three key fit parameters: cutoff length (which sets the maximum range of fractal correlations), fractal dimension (which is indicative of the dimensionality of the magnetic correlations), and magnetic radius (which approximates the structural radius here). Note that the cutoff length values peak at 100 K, with a length scale of ≈ 25 nm indicating a range of correlations that can extend across several nanoparticles. Furthermore, as temperature decreases, the fitted fractal dimension d is observed to change from one to two dimensions, consistent with

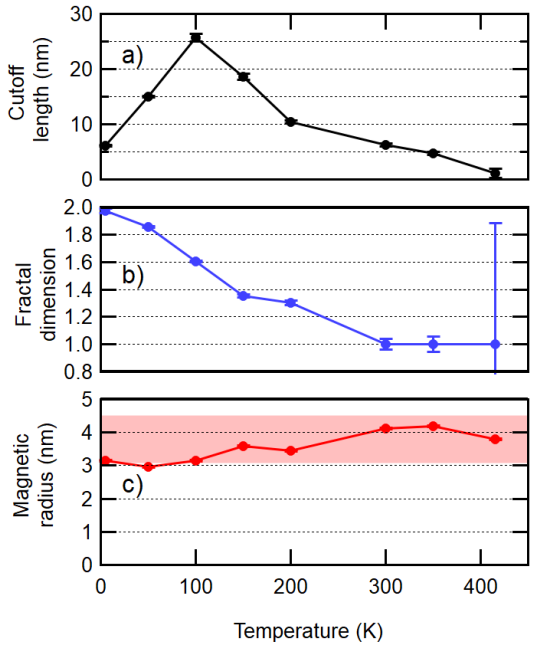


FIG. 7. Plot of a) cutoff length b) fractal dimension and c) magnetic radius vs. temperature in fits to Fig. 5 magnetic scattering intensity data. Shaded red region in c) indicates the structural radius and uncertainty of 3.8 ± 0.7 nm from TEM measurements. The mass fractal model becomes unphysical for 415 K, with a simple sphere model more representative. Error bars represent standard deviations from the fits.

the change in slope in the data as the intensity varies as $\sim Q^{-d}$. The intriguing drop in cutoff length as temperature is lowered below 100 K can then be understood in the context of the magnetic clusters also growing into more of a 2D network rather than a 1D chain. They are associated with a smaller maximum length scale which still exceeds a single particle but now has a greater areal extent. In the meantime, the magnetic radius appears to show some slight variation with temperature which may indicate a change in the magnetically active region of the nanoparticle; although not constrained, the fitted value always lies within the expected range based on the TEM size distribution. Note that in Fig. 7, the mass fractal model was also applied to the 415 K data but reached the bounds in which it could be physically interpreted, as the fitted cutoff length of interactions was *smaller* than the magnetic radius, and the model thus became insensitive to the fractal dimension with a value of 1 ± 0.9, indicating that the data are more simply represented by a single, non-interacting particle model.

The mass fractal model also becomes less appropriate for the neutron scattering data in an applied magnetic field, given the strong net parallel magnetization signal depicted in Fig. 5a) which indicates extended magnetic order from nanoparticle to nanoparticle. Instead, we note another intriguing feature of the field-dependent $M_{\perp}^2$ data highlighted in the inset to Fig. 5b) which shows some small Bragg-like peaks similar to the structural and $M_{||,net}^2$ scattering, particularly in the 0.2 T scan. The presence of this Bragg-like peak in the $M_{\perp}^2$ scattering indicates that some magnetization canting extending from nanoparticle to nanoparticle develops in intermediate applied fields.

The observed peaks in $M_{\perp}^2$ are similar to the magnetic interparticle ones observed previously in dense collections of core-shell $Fe_3O_4/Mn_xFe_{3-x}O_4$ nanoparticles [21, 23]. However, for the core-shell particles, the peaks were maximal in large fields and low temperatures in contrast to the current case in which intermediate temperatures and fields are needed to maximize the canted ordering signal.

This scattering also contrasts with that observed in other related systems. For dense $CoFe_2O_4$ assemblies, the perpendicular magnetic scattering component showed only the form factor of single particle scattering, indicating a tilted magnetic order that was not coherent from nanoparticle to nanoparticle in any situation [18]. In the case of Fe_3O_4 ordered assemblies, $M_{\perp}^2$ showed a large dip, rather than peak near the scattering vector associated with the structural ordering; the magnetic form factor matched to that of canted magnetic shells with little evidence of longer range correlations over the field and temperature ranges studied [15, 19].

C. Simulations

The PASANS data in Section III reveal two striking features in the $M_{\perp}^2$ intensity: (1) a magnetic fractal correlation length that maximizes at intermediate temperature in remanent fields and is accompanied by a change in network dimensionality and (2) a magnetic peak at 200 K that is indicative of collective magnetic ordering, such as domain formation, and is most prominent at intermediate fields. To gain further insight into the mechanisms responsible for these features, we performed micromagnetic simulations of our nanoparticle assembly and used the outputs to simulate the corresponding perpendicular magnetic scattering. As mentioned earlier, we focus in particular on the role of anisotropy, as this parameter varies

the most with temperature based on the bulk manganese ferrite behavior [32–34].

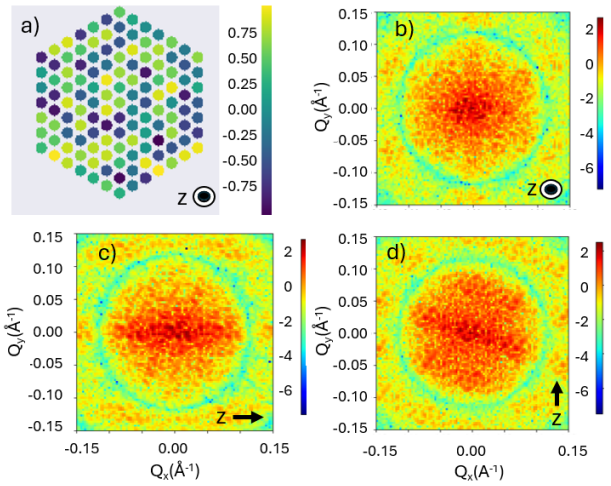


FIG. 8. a) Real space image of the OOMMF output of the middle layer of cluster of nanoparticles showing color scale of z component of magnetization for K=6.75 kJ/m^3, with layer stack defining the z direction. Logarithmic color map of SasView simulations for spin flip scattering using the OOMMF output for the layer stack oriented b) along the neutron beam direction c) along the neutron polarization direction and d) perpendicular to the beam and the neutron polarization direction. Intensity is in arbitrary units set by a simulation scale factor.

Figure 8 shows typical OOMMF and SasView simulation results for specifically magnetization M of 3.57×10^5 A/m, exchange A of 5×10^{-12} J/m, and uniaxial K of 6.75 kJ/m^3 in a weak field of 0.005 T oriented through the 11-layer stack of nanoparticles, where z indicates the stack direction. Within a given nanoparticle, we find nearly the same alignment across the simulation cells, consistent with the fits to the experimental data in Fig. 7c), which mainly match to the full nanoparticle size. From one nanoparticle to the next, however, the alignment is observed to vary quite significantly, likely due to the randomly selected uniaxial anisotropy direction as well as the need to minimize stray fields in remanence. In Fig. 8a), a cut through the middle layer of the simulated nanoparticle assembly reveals this distribution of different moment projections varying from nanoparticle to nanoparticle in the final energy minimized configuration. There are some potential small clusters evidenced by neighboring nanoparticles with similar coloring, which would be consistent with the cutoff length and fractal dimensions indicated in Fig. 7a) and b). However, since the regions are not very large, it is challenging to assess whether they are completely isolated particles, 1D

chains, 2D flakes, 3D structures, or something in between. Since it is difficult to characterize the arrangement from a direct real-space representation, we turn instead to the expected neutron scattering of the collection.

Fig. 8b) shows the spin-flip scattering cross-section for the layer stack arrangement in a) oriented along the assumed neutron beam direction. The simulated scattering has a circular dip at $Q \approx 0.11$ Å^{-1} due to the identical, repeated nanoparticle size and a six-fold symmetric pattern reflecting the perfect symmetry of the layers of stacked hexagons in our idealized nanoparticle FCC crystals. Since our true sample has multiple orientations of nanoparticle polycrystals, we also computed the spin-flip scattering for two other orthogonal orientations of the layer stack, with the stack direction along the polarization direction in Fig. 8c) and orthogonal to both the neutron beam and polarization direction in Fig. 8d). These orientations also display the circular dip associated with the particle size, but the rest of the pattern varies depending on the assembly orientation.

After combining the scattering results from the three orientations and performing a circular average, in Figure 9, we show the simulated magnetic intensity as a function of scattering vector Q for a range of anisotropy values, consistent with previous literature on manganese ferrite [32–34, 48]. The overall I vs. Q curves resemble single particle form factors, but as anisotropy is reduced, longer range correlations appear in increased intensity and an emerging interparticle peak as is seen in the structural data in Fig. 4 and the in-field data in Fig. 5. As shown in the insets to Fig. 9, the simulated scattering pattern resulting from the assembly stack oriented along the beam direction goes from nearly isotropic to highly ordered as anisotropy is decreased from 13.5 kJ/m^3 to 3.0 kJ/m^3. The simulated data in Fig. 9 have been fit to the same mass fractal model as in Fig. 6, but with a fixed radius of 3.8 nm for the particle size and with the addition of a Gaussian peak for the lowest three anisotropy values. When present, the Gaussian peak fits to a peak location of 0.07 Å^{-1} as expected from the simulated nanoparticle array separation.

Figure 10 shows the cutoff length and fractal dimension fit parameters as a function of anisotropy. Note that the cutoff length and fractal dimension parameter changes with anisotropy are very similar to the experimental data parameter changes in Fig. 7 as a function of temperature. In this way, the anisotropy parameter acts as an analogue to temperature in the system. In the case of the simulated data, as anisotropy is decreased, the fractal dimension increases from one dimension towards three, with the cutoff length

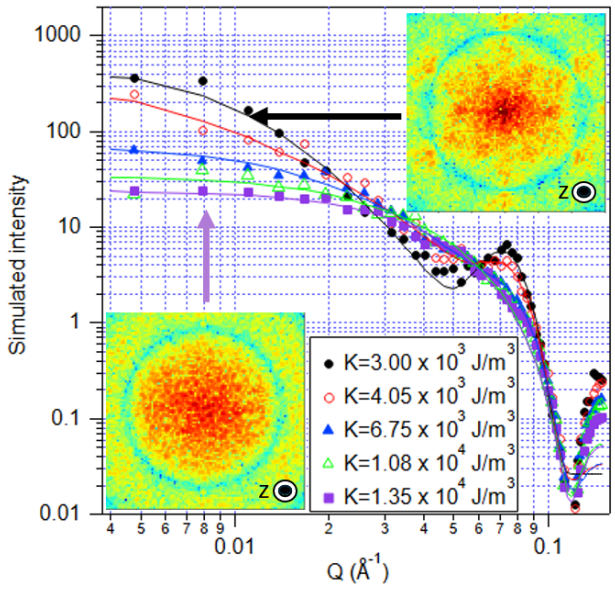


FIG. 9. Simulated magnetic scattering intensity as a function of scattering vector Q for the combined three directions illustrated in Fig. 8b)-d) and circularly averaged for a range of anisotropy values. Simulated data are fit to the same mass fractal model also used for the data in Fig. 6 Representative logarithmic color maps for the extremes of K at 3.0 kJ/m^3 and 13.5 kJ/m^3 are shown as insets, with the same scale range and same simulation scale factor as in Fig. 8b).

growing and then shrinking again as the dimension grows, following the overall shape of Fig. 7. The cutoff lengths are similar in both Fig. 7a) and Fig. 10 a), extending across several nanoparticles, while in the simulations, the fractal dimension parameter extends closer to 3D versus just 2D in the PASANS data and there is also the observed interparticle peak, consistent with a larger degree of ordering for the smallest anisotropies. The greater fractal dimension for the simulation relative to that obtained for the lowest temperature neutron scattering data may be a reflection of the perfect arrangement that has been assumed in the simulation with no stacking faults or defects; alternatively, the relevant anisotropy for the sample at 5 K may not be exactly mimicked by the simulation. Note that the anisotropy values considered in the simulations are physically relevant and match to the range expected for literature values of manganese ferrite [32–34] as well as from considering the blocking temperature behavior in Fig. 3. They are below or at the $\approx$ 13.5 kJ/m^3 considered for Fe_3O_4 [19] and well below the $\approx$ 0.5-2.0 MJ/m^3 considered for $CoFe_2O_4$ [18] nanoparticle assemblies.

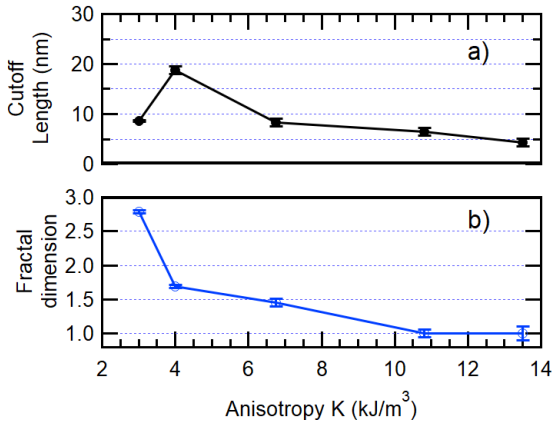


FIG. 10. Plot of a) cutoff length and b) fractal dimension vs. anisotropy in fits to Fig. 9 simulated magnetic scattering intensity data. Error bars represent standard deviations from the fits.

In Figure 11, we plot the simulated spin-flip neutron scattering patterns for a fixed anisotropy value of 6.75 kJ/m^3 and magnetic fields ranging from 0.005 T to 1.0 T, with the field direction within the layer plane of the simulated assembly. Patterns are displayed at representative field values for which qualitative changes are observed. As in Fig. 8b), the neutron beam is oriented along the layer stack direction, with the applied field horizontal. As expected in higher magnetic fields, the neutron scattering patterns display evidence of more complex magnetic ordering with brighter diffraction spots originating from the perfect FCC single crystal structure assumed in the simulation [61].

For these simulations performed in any appreciable magnetic field, it is not possible to easily average over multiple nanoparticle assembly orientations as was done for Fig. 9 because the field direction in the energy-minimized OOMMF simulations must be matched to the neutron polarization direction; the assembly orientation and field direction must be established for each separate micromagnetic simulation. Furthermore, the two perpendicular to the field Fourier transform components, $|M_Y(\vec{Q})|^2$ and $|M_Z(\vec{Q})|^2$, may not be equal in these field-dependent simulations, as the arrangements in the layer stack direction and within the layer plane are not entirely identical.

With these caveats in mind, we can still compute the spin-flip cross-section sum from Eq. 3, but with the value representing an averaged perpendicular magnetic scattering component with $|M_Z(\vec{Q})|^2$ and $|M_Y(\vec{Q})|^2$ not necessarily equal. As shown in Figure 12, while these simulation results are noisier than the remanent ones of Fig. 9, we can still observe simi-

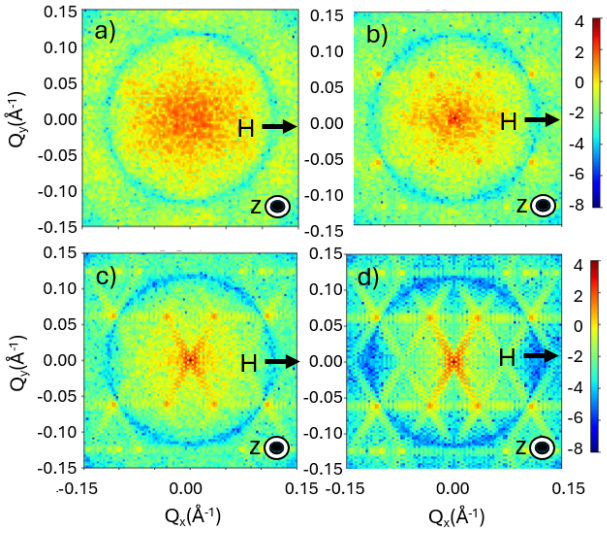


FIG. 11. Logarithmic color map of SasView-generated neutron scattering patterns for spin flip scattering using a nanoparticle assembly with K=6.75 kJ/m^3 in a) remanence (0.005 T), b) 0.05 T, c) 0.1 T, and d) 1.0 T with field oriented horizontal along X to match the geometry of Fig. 1. Intensity is set by the same simulation scale factor as in Figs. 8 and 9.

larities to the PASANS data depicted in Fig. 5b). In moderate fields of 0.1 T and above, a peak-like structure emerges at the interparticle peak, again indicating some correlated canted spin component beyond those that align in the field.

In contrast to the experimental work shown in Fig. 5b), however, the peak persists at higher field and the overall signal strength, while weakening with field, is more robust. For these simulations, the particles are uniform and arranged uniformly with only one crystalline orientation such that magnetic ordering features are likely to be more prominent relative to the experimental data. While there is no explicit match to the observed scattering, the simulations show a canted extended structure in a moderate field is possible for the energy parameters we used based on bulk manganese ferrite and the magnetometry measurements.

IV. SUMMARY AND CONCLUSIONS

In summary, we have used advanced PASANS methods to directly probe the spin structures in ordered, chemically homogeneous manganese ferrite nanoparticle assemblies, and we have connected our observations with micromagnetic simulations coupled to simulated neutron scattering patterns. We find that a mass fractal model of clusters of nanoparticles can

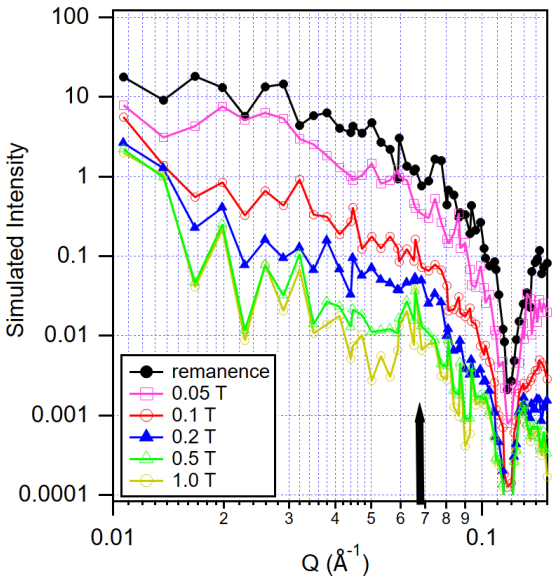


FIG. 12. Simulated perpendicular magnetic scattering intensity from Eq. 3 as a function of scattering vector Q for different values of applied field, taken from simulation data illustrated in Fig. 11 for select fields with K=6.75 kJ/m^3.

be used to explain the experimental *and* simulated data in remanence with dimensionality increasing with decreasing temperature and anisotropy, respectively. Moderate adjustments of the magnetic anisotropy constant have a dramatic effect on the energy-stabilized spin structures, spanning from isolated magnetic sphere behavior to that of correlated fractal clusters of several nanoparticles extended in two to three dimensions. In addition, field-dependent changes in the simulations mimic the experimental observations of domains.

Instead of the usual explanation of blocking temperature behavior for superparamagnetic particles, we interpret the role of anisotropy in a different fashion. The observed crossover temperature of $\approx$ 50-100 K in the remanent magnetic scattering is attributed to the formation of local magnetically correlated fractal clusters of particles with a characteristic cutoff length and fractal dimension driven by the balance between anisotropy and dipolar energies. In both the data and simulations, the correlation length is maximized at an intermediate fractal dimension of $\approx$ 1.5. This interpretation is similar to that described recently by [10] in which the behavior of a dilute solution of particles is dictated by a small amount of clustering, leading to an effective interaction temperature. Here, we directly study magnetic cluster formation in a structurally ordered system of surfactant-separated nanoparticles. In an ap-

plied magnetic field, the fractal magnetic network reverts towards a more standard domain configuration, albeit with a perpendicular component of magnetization that is surprisingly correlated over large distances for intermediate fields.

The manganese ferrite nanoparticles studied here display a pronounced anisotropy sensitivity to determining *interparticle* magnetic structures compared to the *intraparticle* ones observed in the related systems of Fe_3O_4 and $CoFe_2O_4$ nanoparticles [15, 18, 19]. Unlike the core-shell $Fe_3O_4/Mn_xFe_{3-x}O_4$ nanoparticles which showed persistent correlated canted structures [21, 23], these homogeneous assemblies display a wider, more tunable array of morphologies, ranging from single particle to fractal clusters to extended domains.

It is important to acknowledge some limitations of the work presented here. Our simulations assume a perfect lattice of nanoparticles of exactly the same size, with each nanoparticle represented by cube-shaped cells with specific parameters for magnetization, anisotropy, and exchange rather than the actual atomic sites. The true physical system has a size distribution as well as spacing and defect variations which could significantly modify the magnetic domain or network formation. The cell size is also critical for the neutron scattering simulations, as this dimension fundamentally sets a limit to the highest scattering vector Q that can be computed. Greater cell discretization, however, might not be necessary in this case, given the soft magnetic character of the manganese ferrite nanoparticles. Further improvements could be made to implement more robust orientational averaging of multiple OOMMF-generated spin configurations in the SasView software.

Looking to the future, we note that in addition to the generic scattering calculator used here [49], there are other more recent computational approaches to simulate small-angle neutron scattering such as the mag2exp [62] and NuMagSANS [63], the latter of which makes use of GPU acceleration for faster computation. Still, the method used here is quite attractive for this study and integrates well with the experimental results. The data and analysis shown here provide further evidence of the wide range of magnetic nanoparticle spin structures that may be adopted, depending on the delicate balance of the competing energetics in the composite systems.

ACKNOWLEDGMENTS

We thank W.C. Chen, S.M. Watson, and H. Burrall for their assistance with the polarized ^{3}He spin filters. Access to the vSANS instrument at the NIST Center for Neutron Research was provided by the Center for High Resolution Neutron Scattering, a partnership between the National Institute of Standards and Technology and the National Science Foundation (NSF) under Agreement No. DMR-2010792. This work was partially supported by NSF DMR-1606887 and an Oberlin College Research Status Award and made use of the Oberlin high performance computing cluster obtained through NSF DBI-1427949. H. Chen and S. A. Majetich acknowledge support by the Department of Energy through grant #DE-SC0019237. We also acknowledge support from EPSRC (Grant No. EP/S033394/1). This work benefited from the use of the SasView application, originally developed under NSF Award DMR - 0520547. SasView also contains code developed with funding from the EU Horizon 2020 programme under the SINE2020 project Grant No 654000.

DATA AVAILABILITY

The neutron scattering data that support the findings of this study are available at [64]. The remaining data are available from the corresponding author upon reasonable request.

[1] Z. Ma, J. Mohapatra, K. Wei, J. P. Liu, and S. Sun, Magnetic nanoparticles: synthesis, anisotropy, and applications, Chem. Rev. **1**, c00860 (2021).

[2] X. Batlle, C. Moya, M. Escoda-Torroella, Ò. Iglesias, A. Fraile Rodríguez, and A. Labarta, Magnetic nanoparticles: from the nanostructure to the physical properties, J. Magn. Magn. Matl. **543**, 168594 (2022).

[3] Z. Z. Bandic and R. H. Victora, Advances in magnetic data storage technologies, Proc. IEEE **96**, 1749 (2008).

[4] K. Krishnan, Biomedical nanomagnetics: a spin through possibilities in imaging, diagnostics, and therapy, IEEE Trans. Magn. **46**, 2523 (2010).

[5] S. A. Majetich, T. Wen, and O. T. Mefford, Magnetic nanoparticles, MRS Bull. **38**, 899 (2013).

[6] L. Mohammed, H. G. Gomaa, D. Ragab, and J. Zhu, Magnetic nanoparticles for environmental and biomedical applications: a review, Particuology **30**, 1 (2017).

[7] N. Neugebauer, Y. Wang, M. T. Elm, D. M. Hofmann, C. Heiliger, X. Ye, and P. J. Klar, Distance and size dependence of the interactions within highly ordered magnetic nanoparticle mesocrystals, Phys. Rev. B **107**, 184410 (2023).

[8] J. Mohapatra, P. Joshi, H. Abbas, M. Gusenbauer, K. Bian, P. Lu, H. Fan, T. Schrefl, and J. P. Liu, Superstructure magnetic anisotropy in Fe_3O_4 nanoparticle chains, Nat. Comm. **16**, 5723 (2025).

[9] C. Kons, H. Srikanth, M.-H. Phan, D. A. Arena, and M. Pereiro, Macrospin model of an assembly of magnetically coupled core-shell nanoparticles, Phys. Rev. B **106**, 104402 (2022).

[10] R. E. Camley, R. Macêdo, and K. L. Livesey, Curie-weiss behavior and the interaction temperature of magnetic nanoparticle ensembles: Local structure strongly affects the magnetic behavior, Phys. Rev. B **110**, 144440 (2024).

[11] A. Wiedenmann, Small angle neutron scattering investigations of magnetic nanostructures using polarized neutrons, J. Appl. Cryst. **33**, 428 (2000).

[12] I. Bergenti, A. Deriu, L. Savini, E. Bonetti, F. Spizzo, and H. Hoell, Small angle polarised neutron scattering investigation of magnetic nanoparticles, J. Magn. Magn. Matl. **262**, 60 (2003).

[13] S. M. Yusuf, J. M. DeTeresa, M. D. Mukadam, J. Kohlbrecher, M. R. Ibarra, J. Arbiol, P. Sharma, and S. K. Kulshreshtha, Experimental study of the structural and magnetic properties of gamma-Fe_2O_3 nanoparticles, Phys. Rev. B **74**, 224428 (2006).

[14] K. Theis-Bröhl, M. Wolff, I. Ennen, C. D. Dewhurst, A. Hütten, and B. P. Toperverg, Self ordering of nanoparticles in magneto-organic composite films, Phys. Rev. B **78**, 134426 (2008).

[15] K. L. Krycka, R. A. Booth, C. R. Hogg, Y. Ijiri, J. A. Borchers, W. C. Chen, S. M. Watson, M. Laver, T. R. Gentile, L. R. Dedon, S. Harris, J. J. Rhyne, and S. A. Majetich, Core-shell magnetic morphology of structurally uniform magnetite nanoparticles, Phys. Rev. Lett. **104**, 207203 (2010).

[16] P. K. Manna, S. M. Yusuf, M. D. Mukadam, and J. Kohlbrecher, Evidence of a core-shell structure in the antiferromanget $La_{0.2}Ce_{0.8}CrO_3$ nanoparticles by neutron scattering, Appl. Phys. A **109**, 385 (2012).

[17] K. L. Krycka, J. A. Borchers, M. Laver, G. Salazar-Alvarez, A. López-Ortega, M. Estrader, S. Suriñach, M. D. Baró, J. Sort, and J. Nogués, Correlating material-specific layers and magnetic distributions within onion-like Fe_3O_4/MnO/γ-Mn_2O_3 core/shell nanoparticles, J. Appl. Phys. **113**, 17B531 (2013).

[18] K. Hasz, Y. Ijiri, K. L. Krycka, J. A. Borchers, R. A. Booth, S. Oberdick, and S. A. Majetich, Particle moment canting in $CoFe_2O_4$ nanoparticles, Phys. Rev. B **90**, 180405(R) (2014).

[19] K. L. Krycka, J. A. Borchers, R. A. Booth, S. A. Majetich, Y. Ijiri, K. Hasz, and J. J. Rhyne, Origin of surface canting within Fe_3O_4 nanoparticles, Phys. Rev. Lett. **113**, 147203 (2014).

[20] X. Sun, A. Klapper, Y. Su, K. Nemkovski, A. Wildes, H. Bauer, O. Köhler, A. Schilmann, W. Tremel, O. Petracic, and T. Brückel, Magnetism of monomer MnO and heterodimer FePt@MnO nanoparticles, Phys. Rev. B **95**, 134427 (2017).

[21] S. D. Oberdick, A. Abdelgawad, C. Moya, S. Mesbahi-Vasey, D. Kepaptsoglou, V. K. Lazarov, R. F. L. Evans, D. Meilak, E. Skoropata, J. van Lierop, I. Hunt-Isaak, H. Pan, Y. Ijiri, K. L. Krycka, J. A. Borchers, and S. Majetich, Spin canting across core/shell $Fe_3O_4/Mn_xFe_{3-x}O_4$ nanoparticles, Sci. Rep. **8**, 3425 (2018).

[22] P. Bender, E. Wetterskog, D. Honecker, J. Fock, C. Frandsen, C. Moerland, L. K. Bogart, O. Posth, W. Szczerba, H. Gavilán, R. Costo, M. T. Fernández-Díaz, D. González-Alonso, L. Fernández-Barquín, and C. Johansson, Dipolar-coupled moment correlations in clusters of magnetic nanoparticles, Phys. Rev. B **98**, 224420 (2018).

[23] Y. Ijiri, K. L. Krycka, I. Hunt-Isaak, H. Pan, J. Hsieh, J. A. Borchers, J. J. Rhyne, S. D. Oberdick, A. Abdelgawad, and S. A. Majetich, Correlated spin canting in ordered core-shell $Fe_3O_4/Mn_xFe_{3-x}O_4$ nanoparticle assemblies, Phys. Rev. B **99**, 094421 (2019).

[24] D. Honecker, L. Fernández Barquín, and P. Bender, Magnetic structure factor of correlated moments in small-angle neutron scattering, Phys. Rev. B **101**, 134401 (2020).

[25] R. M. Moon, T. Riste, and W. C. Koehler, Polarization analysis of thermal neutron scattering, Phys. Rev. **181**, 920 (1969).

[26] K. L. Krycka, J. Borchers, Y. Ijiri, R. A. Booth, and S. Majetich, Polarization-analyzed small-angle neutron scattering. II. mathematical angular analysis, J. Appl. Cryst. **45**, 554 (2012).

[27] D. Honecker, A. Ferdinand, F. Döbrich, C. D. Dewhurst, A. Wiedenmann, C. Gómez-Polo, K. Suzuki, and A. Michels, Longitudinal polarization analysis in small-angle neutron scattering, Eur. Phys. J. B **76**, 209 (2010).

[28] C. Liu, B. Zou, A. Rondinone, and Z. J. Zhang, Reverse micelle synthesis and characterization of superparamagnetic $MnFe_2O_4$ spinel ferrite nanocrystallites, J. Phys. Chem. B **104**, 1141 (2000).

[29] A. López-Ortega, M. Estrader, G. Salazar-Alvarez, S. Estradé, I. V. Golosovsky, R. K. Dumas, D. J. Keavney, M. Vasilakaki, K. N. Trohidou, J. Sort, F. Peiró, S. Suriñach, M. D. Baró, and J. Nogués, Strongly exchange coupled inverse ferrimagnetic soft/hard, $Mn_xFe_{3-x}O_4/Fe_xMn_{3-x}O_4$, core/shell heterostructured nanoparticles, Nanoscale **4**, 5138 (2012).

[30] K. Vamvakidis, D. Sakellari, M. Angelakeris, and C. Dendrinou-Samara, Size and compositionally controlled manganese ferrite nanoparticles with enhanced magnetization, J. Nanoparticle Res. **15**, 1743 (2013).

[31] Y.-K. Li, L. Cheng, X.-D. Zhang, and X. Guo, Hierarchically-structured $MnFe_2O_4$ nanospheres for highly sensitive detection of NO_2, Solid State Ionics **336**, 102 (2019).

[32] N. Miyata, Ferromagnetic crystalline anisotropy of $MnFe_2O_4$-Fe_3O_4 ferrite solid solutions, Journal of the Physical Society of Japan **16**, 1291 (1961).

[33] W. Palmer, Low temperature anisotropy of manganese iron ferrites, J. Appl. Phys. **33**, 1201 (1962).

[34] Z. Simsa and V. Brabers, Influence of the degree of inversion on magnetic properties of $MnFe_2O_4$, IEEE Transactions on Magnetics **11**, 1303 (1975).

[35] S. Sun, H. Zeng, D. B. Robinson, S. Raoux, P. M. Rice, S. X. Wang, and G. Li, Monodisperse MFe_2O_4 (M = Fe, Co, Mn) nanoparticles, J. Am. Chem. Soc. **126**, 273 (2004).

[36] D. V. Talapin, E. V. Shevchenko, A. Kornowski, N. Gaponik, M. Haase, A. L. Rogach, and H. Weller, A new approach to crystallization of CdSe nanoparticles into ordered three-dimensional superlattices, Adv. Matl. **13**, 1868 (2001).

[37] D. F. Farrell, Y. Ijiri, C. V. Kelly, J. A. Borchers, J. J. Rhyne, Y. Ding, and S. A. Majetich, Small angle neutron scattering study of disordered and crystalline iron nanoparticle assemblies, J. Magn. Magn. Mater **303**, 318 (2006).

[38] D. Farrell, Y. Chen, S. Kan, M. Sachan, Y. Ding, S. A. Majetich, and L. Yang, Iron nanoparticle assemblies: structures and magnetic behavior, J. Phys. Conf. Ser. **17**, 185 (2005).

[39] S. A. Majetich and M. Sachan, Magnetostatic interactions in magnetic nanoparticle assemblies: energy, time and length scales, J. Phys. D **39**, R407 (2006).

[40] K. L. Krycka, R. Booth, J. A. Borchers, W. C. Chen, C. Conlon, T. R. Gentile, C. Hogg, Y. Ijiri, M. Laver, B. B. Maranville, S. A. Majetich, J. J. Rhyne, and S. M. Watson, Resolving 3D magnetism in nanoparticles using polarization analyzed SANS, Physica B **404B**, 251 (2009).

[41] W. C. Chen, R. Erwin, J. W. M. III, S. Watson, C. B. Fu, T. R. Gentile, J. A. Borchers, J. W. Lynn, and G. L. Jones, Applications of ^{3}He neutron spin filters at the ncnr, Physica B **404B**, 2663 (2009).

[42] K. L. Krycka, W. Chen, J. Borchers, B. Maranville, and S. Watson, Polarization-analyzed small-angle neutron scattering. I. polarized data reduction using pol-corr, J. Appl. Cryst. **45**, 546 (2012).

[43] Note in Eq. 3, the term $|M_Y(\vec{Q}, 90°)|^2$ is absent due to neutron selection rules which prohibit it from being observed in the spin-flip intensities $I^{+-}_{\theta=90°}(\vec{Q})$ and $I^{-+}_{\theta=90°}(\vec{Q})$ as described in [26]. Also, note if the scattering in the two perpendicular directions were not equivalent, e.g. $|M_Y(\vec{Q})|^2 \neq |M_Z(\vec{Q})|^2$, Eq. 3 would still hold, relating the intensities and Fourier transform components, but with the quantity equal to now $|M_{\perp,yz\,avg}|(\vec{Q})|^2$, an averaged version of the perpendicular magnetic components.

[44] M. Beg, M. Lang, and H. Fangohr, Ubermag: Towards more effective micromagnetic workflows, IEEE Trans. Magn. **58**, 1 (2022).

[45] M. J. Donahue and D. G. Porter, *OOMMF User's Guide, Version 1.0*, Tech. Rep. Interagency Report NISTIR 6376 (National Institute of Standards and Technology, 1999).

[46] J. Smit and H. P. J. Wijn, *Ferrites* (Philips Technical Library, Eindhoven, 1959) p. 157.

[47] Y. V. Velikanova, M. R. Vinogradova, L. A. Mitlina, and N. V. Meleshko, Exchange spin waves in inhomogeneous spinel ferrite films, Inorg. Mater. **54**, 667 (2018).

[48] S. Yoon and K. M. Krishnan, Temperature dependence of magnetic anisotropy constant in manganese ferrite nanoparticles at low temperature, J. Appl. Phys. **109**, 07B534 (2011).

[49] J. Krzywon *et al.*, Sasview version 6.1.2 10.5281/zenodo.17795298 (2025).

[50] In the core-shell particles, the Fe_3O_4 nucleated first due to the lower decomposition temperature of the iron precursor; as temperature was increased in the synthesis process, the manganese precursor then decomposed, leading to a Mn-rich shell.

[51] R. Nepal, M. Saghayezhian, J. Zhang, and R. Jin, Observation of three magnetic states in spinel $MnFe_2O_4$ single crystals, J. Magn. Magn. Matl. **497**, 165955 (2020).

[52] A. Guinier and G. Fournier, *Small-Angle Scattering of X-rays* (John Wiley and Sons, 1955) p. 55.

[53] https://www.sasview.org/docs/user/models/sphere.html (2025).

[54] D. F. R. Mildner and P. L. Hall, Small-angle scattering from porous solids with fractal geometry, J. Phys. D: Appl. Phys. **19**, 1535 (1986).

[55] https://www.sasview.org/docs/user/models/mass_ fractal.html (2025).

[56] This unusual temperature dependence was verified in a separate data run with the data taken in a different sequence to eliminate the possibility of a time-related, hysteresis effect.

[57] T. Freltoft, J. K. Kjems, and S. K. Sinha, Power-law correlations and finite-size effects in silica particle aggregates studied by small-angle neutron scattering, Phys. Rev. B **33**, 269 (1986).

[58] A. Taufiq, Sunaryono, E. G. R. Putra, A. Okazawa, I. Watanabe, N. Kojima, S. Pratapa, and Darminto, Nanoscale clustering and magnetic properties of $Mn_xFe_{3-x}O_4$ particles prepared from natural magnetite, J. Superconductivity and Novel Magn. **28**, 2855 (2015).

[59] E. G. R. Putra, B. S. Seong, E. Shin, A. Ikram, S. A. Ani, and Darminto, Fractal structures on Fe_3O_4 ferrofluid: a small-angle neutron scattering study, J. Phys. Conf. Ser. **247**, 012028 (2010).

[60] N. Tang, W. L. N. C. Liyanage, S. A. Montoya, S. Patel, L. J. Quigley, A. J. Grutter, M. R. Fitzsimmons, S. Sinha, J. A. Borchers, E. E. Fullerton, L. DeBeer-Schmitt, and D. A. Gilbert, Skyrmion-excited spin-wave fractal networks, Adv. Mater. **35**, 2300416 (2023).

[61] Asymmetry in the high field simulation patterns reflects the neutron scattering vector selection rules.

[62] S. J. R. Holt, M. Lang, J. C. Loudon, T. J. Hicken, D. Suess, D. Cortés-Ortuño, S. A. Pathak, M. Beg, K. Zulfiqar, and H. Fangohr, Virtual experiments in computational magnetism with mag2exp, npj Comp. Matl. **11**, 201 (2025).

[63] M. P. Adams and A. Michels, *NuMagSANS*: a GPU-accelerated open-source software package for the generic computation of nuclear and magnetic small-angle neutron scattering observables of complex systems, J. Appl. Cryst. **59**, 943 (2026).

[64] https://ncnr.nist.gov/pub/ncnrdata/vsans/202001/25934/ (2020).